

Article

An Investigative Study for the Seismic Performance of Composite-Reinforced Masonry Wall with Prestressing Technology

Bin Chi ^{1,*}, Yuhu Quan ², Fenglai Wang ²  and Xu Yang ² ¹ School of Civil Engineering, Suzhou University of Science and Technology, Suzhou 215011, China² School of Civil Engineering, Harbin Institute of Technology, Harbin 150090, China; yuhu.quan@hit.edu.cn (Y.Q.)

* Correspondence: usts-tmcb@mail.usts.edu.cn

Abstract: Prestressing technology is an effective way to improve the seismic performance of masonry structures such as concrete masonry wall. Therefore, bonded prestressing technology applied to integrated concrete masonry wall (ICMW) was proposed in this study, and a cyclic loading test on specimens with different section types was conducted. It was found that the prestressing technology rendered thinner and denser cracks on the load-bearing component of the specimens, while the failure mode remained unchanged. The prestressing technology increased the initial stiffness of the specimens and accelerated their stiffness degradation. Although the prestressing technology advanced the yield displacement of the specimens, it had a positive influence on the displacement ductility of the specimens. Additionally, the energy dissipation of the specimens increased with the deepening of the damage state, while the influence of the prestressing on the energy dissipation of the specimens decreased with an increased in the drift ratio. Furthermore, the equivalent viscous damping of the specimens with a rectangular and T-shaped section finally converged at 8% and 14%, respectively. Overall, the aforementioned findings indicate that the prestressing technology proposed in this study is a useful method for improving the damage propagation and seismic performance of ICMW, which could be used to construct low-rise masonry structures in the future.

Keywords: masonry wall; prestressing technology; cyclic loading; seismic performance; damage propagation



Citation: Chi, B.; Quan, Y.; Wang, F.; Yang, X. An Investigative Study for the Seismic Performance of Composite-Reinforced Masonry Wall with Prestressing Technology. *Buildings* **2024**, *14*, 264. <https://doi.org/10.3390/buildings14010264>

Academic Editors: Matija Gams, Tomislav Kišiček, Roberto Capozucca, Erica Magagnini and Marko Marinković

Received: 17 December 2023

Revised: 10 January 2024

Accepted: 17 January 2024

Published: 18 January 2024



Copyright: © 2024 by the authors. Licensee MDPI, Basel, Switzerland. This article is an open access article distributed under the terms and conditions of the Creative Commons Attribution (CC BY) license (<https://creativecommons.org/licenses/by/4.0/>).

1. Introduction

Masonry is a low-cost, load-bearing material that is simple to construct with; therefore, it has been used widely worldwide. However, traditional masonry structures have been found to be prone to cracking, and they can collapse in earthquakes [1,2]. As shown in Figure 1, the unpredictable failure mode and poor reparability of concrete masonry structures have resulted in a significant number of fatalities and infrastructural losses [3]. Hence, the development of low-cost masonry structures with acceptable seismic performances is a continuously noteworthy research direction.



Figure 1. Damage phenomenon of concrete block masonry structure due to earthquake.

Concrete masonry wall (CMW), as the main load-bearing component used in masonry structures, has been extensively studied in an attempt to improve its seismic performance [4–15]. Janaraj and Dhanasekar [6] proposed two forms of a reinforced grout confining system for CMW; they concluded that the addition of grout into the cores increased the load capacity of unreinforced CMW. Bolhassani et al. [8] tested the seismic performance of partially grouted CMW, and they found that the damage propagation and mechanical mechanism of the partially grouted CMW were similar to that of masonry in-filled reinforced concrete frames. Moreover, Shedid et al. [11] investigated the seismic performance of fully grouted CMW; their results demonstrated that the seismic performance of fully grouted CMW was similar to that of reinforced concrete shear wall. Similar conclusions have also been drawn by Voon and Ingham [12], Zhang et al. [13], and Seif Eldin et al. [14,15], who indicated that fully grouted CMW can be applied in high-rise buildings. The above research has demonstrated that CMW can provide sufficient seismic reserves as the main load-bearing component in practical structures. However, research on the interaction of the in-fill and load-bearing components in masonry structures is scarce, whereas this interaction in reinforced concrete structures has received much attention [16,17]. Therefore, Chi et al. [18] proposed a novel integrated concrete masonry wall (ICMW) based on the concept of “assumed failure infilled masonry” proposed by Markulak et al. [19]. As shown in Figure 2a, the overall masonry wall was divided into three zones according to its functional properties: two fully grouted CMWs comprised the load-bearing component (dark zone), ungrouted CMW comprised the in-fill component (gray zone), and two lightweight autoclaved aerated concrete (AAC) block walls comprised the weak plane (white zone). Based on the experimental results, it was concluded that the in-fill component could be protected by allowing for appropriate time separation, ensuring that the ductility coefficient of the load-bearing component did not decrease. For the damage pattern of ICMW, the crack propagation of the load-bearing component was enhanced by the in-fill component, resulting in masonry block face spalling, as shown in Figure 2b. Notably, the masonry block face spalling of the wall was unpredictable and needs to be either improved upon or avoided in practical engineering.

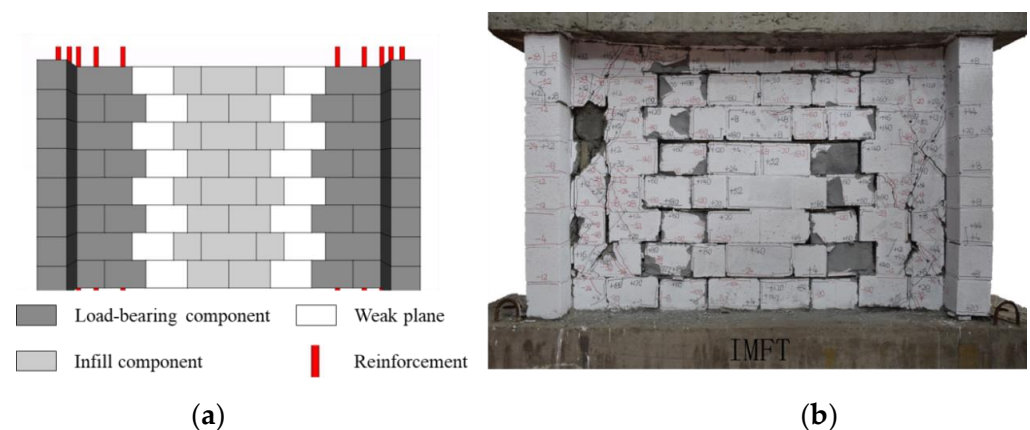


Figure 2. The description of ICMW system adopted from Chi et al. [18]: (a) schematic of ICMW system and (b) serious damage to ICMW system.

Therefore, there are several methods that are commonly applied to overcome the shortcomings of CMW. For example, many high-ductility materials have been proposed and applied on both sides of walls to improve the damage propagation of specimens, such as textile-reinforced mortars [20,21], highly ductile fiber-reinforced concrete [3], and grout-injected ferrocement overlay [22–24]. On the other hand, prestressing technology can also be applied to enhance the seismic performance of CMW [25–32]. Hassanili et al. [26] investigated the seismic performance of unbonded post-tensioned CMW and concluded that the slender specimen showed a rocking response. Guo et al. [32] proposed a prestressing technology used in ring beam and constructional columns to confine masonry wall.

The experimental results showed that post-tensioning had a significant influence on the occurrence of cracks on the walls. Moreover, some improvement methods like replaceable energy dissipation [33–35] and rubber interfaces [36] have also been proposed to improve the deformation behavior of CMW. However, most of the abovementioned methods were unbonded prestressing technology, meaning that the duct needed to be arranged in advance during construction. Research on CMW with bonded prestressing technology was conducted by Rosenboom and Kowalsky [27]; in their study, however, the deformation and strength of the walls were reduced because of the weak interface between the post-tension duct and grouted concrete. Therefore, reasonably setting the interface between prestressed bars and grouted concrete has become key when applying bonded prestressing technology to CMW, which can be used to improve the load-bearing component of ICMW.

This paper details a series of studies on the seismic performance of ICMW, specifically an experimental procedure of ICMW using prestressing technology. Two comparison specimens were constructed and subjected to reverse cyclic loading. The crack propagation, failure pattern, and other seismic performance parameters of the specimens were extensively analyzed and discussed based on the results of this paper and previous research results. The findings detailed herein will provide a technical basis for the application of an ICMW system or other similar types of masonry structures.

2. Experiment Program

2.1. Test Specimens and Construction

As shown in Figure 3, the overall height of the specimen was 2700 mm, while a top beam with a height of 400 mm and a bottom beam with a height of 700 mm were poured with the wall to provide end constraints. Two wall section types were constructed to investigate the influence of flanges on the seismic performance of the specimen. The specimens were divided into three functional zones, namely a load-bearing component composed of fully grouted CMWs, an in-fill component composed of ungrouted CMWs, and a weak plane composed of AAC blocks. To enhance the interaction between the load-bearing component and in-fill component, AAC blocks were placed in the shape of teeth; meanwhile, two plain bars were placed at the mortar layer of the ungrouted CMW and anchored in the fully grouted CMWs. To make comparisons with previous research, these specimens adopted a similar naming principal in Chi et al.'s study [18], where the symbol P was introduced to represent prestressing technology. Therefore, the specimen with a rectangular section was named IMFP, while that with a T-shaped section was named IMFTP. Detailed configuration information of the two specimens can be found in Figure 3 and Table 1.

For prestressing technology, a bonded prestressing technology was proposed, and the construction details are outlined in Figure 4. It should be noted that the prestressing technology was used to improve the damage propagation of the load-bearing component of the ICMW; therefore, the amplitude of the prestress would not be larger, which was only applied on the section of the load-bearing component compared to that of the entire wall. As shown in Figure 4a, the vertical bars in the load-bearing component acted as prestressed bars simultaneously. One end of the bars was anchored to the bottom beam, while the other was premachined with threads. Figure 4c,d highlight the prestressing positions of the specimen with blue regions. The prestressed bars were symmetrically distributed at both ends of the load-bearing component, and the moment balance at the center of the section of fully grouted CMW was considered. To facilitate the construction and ensure the effectiveness of prestress, the magnitude of the prestress of each fully grouted CMW was set as 0.453 MPa, corresponding to the design axial compression ratio of 0.1, which was in accordance with GB 50003-2011 [37]. The detailed calculation process and results of the tensile stress of the vertical bars are shown in Table 2.

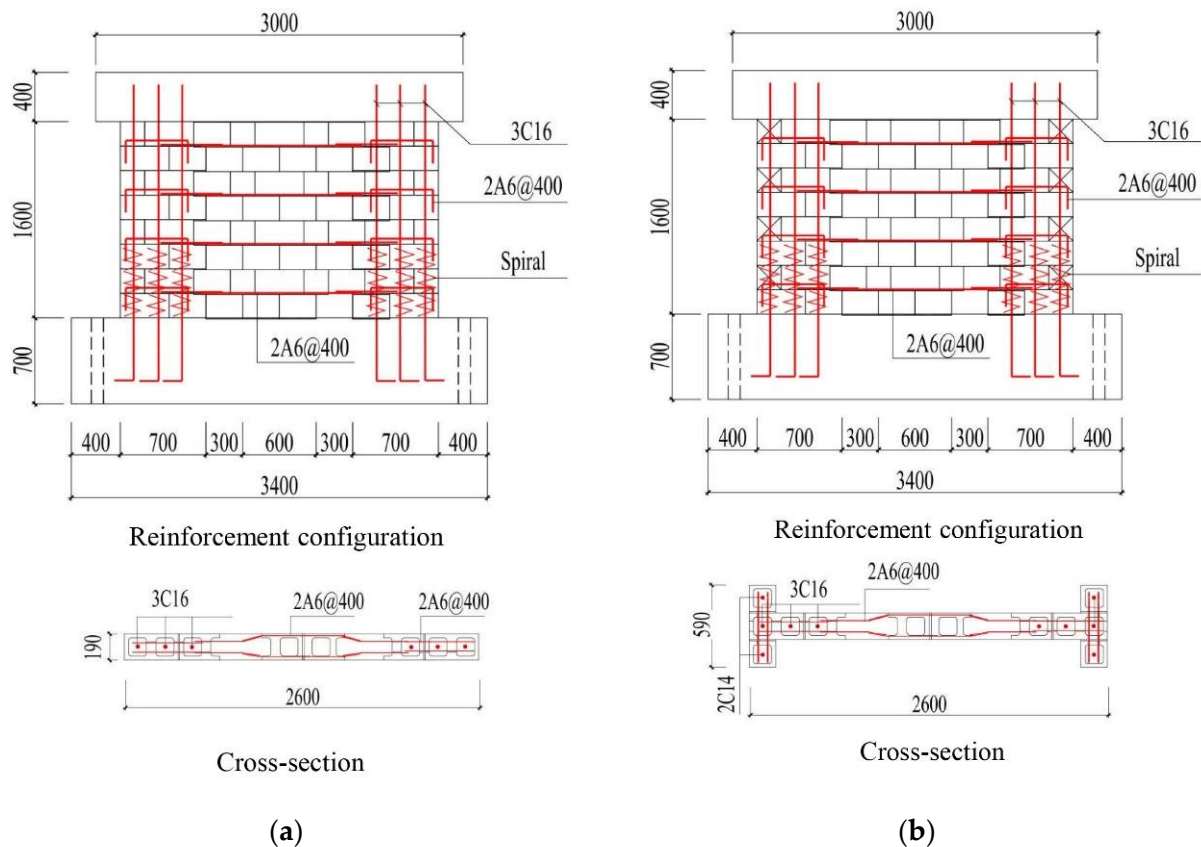


Figure 3. Configuration of all specimens (dimensions in mm): (a) schematic of IMFP; (b) schematic of IMFTP.

Table 1. Configuration information of specimens.

Specimen	Load-Bearing				In-Fill Length (mm)	Reinforcement Configuration			Prestress (MPa)
	Length (mm)	Width (mm)	Height (mm)	Flange (mm)		Vertical	Horizontal	Spiral	
IMFP	590	190	1600	0	600	6C16	2A6@400	A6@70	0.453
IMFTP	590	190	1600	590	600	4C14 + 6C16	2A6@400	A6@70	0.453

Note: A represents reinforcement strength grade HPB 235 with standard yield strength of 235 MPa, and C represents reinforcement strength grade HRB 400 with standard yield strength of 400 MPa.

A construction plan of prestressing technology was tested in this experiment. As shown in Figure 5, hollow CMWs and bottom beams were separately prefabricated first; meanwhile, horizontal and vertical bars were arranged in the hollow CMWs and bottom beams, respectively. Then, the hollow CMWs were fastened and lifted for installation on the bottom beam. Steel struts were used to fix and vertically adjust the wall simultaneously, while AAC blocks were constructed in the tooth gaps between the hollow CMWs. Third, as vertical bars were inside the holes of hollow CMWs, anchorage plates were installed at the top face of the hollow CMWs. The ends of those bars were fixed by the anchorage plate and screw nuts using a torque wrench. It should be noted that the magnitude of the torque was set in advance to ensure that the magnitudes of stress and the strain variations in certain vertical bars were also monitored in real-time to ensure the effectiveness of the prestressing technology. After that, fine-aggregate concrete with an initial slump of 180 mm was used to grout the hollow CMWs of the load-bearing component, and top beams were constructed. All the specimens were cured in an appropriate environment before testing.

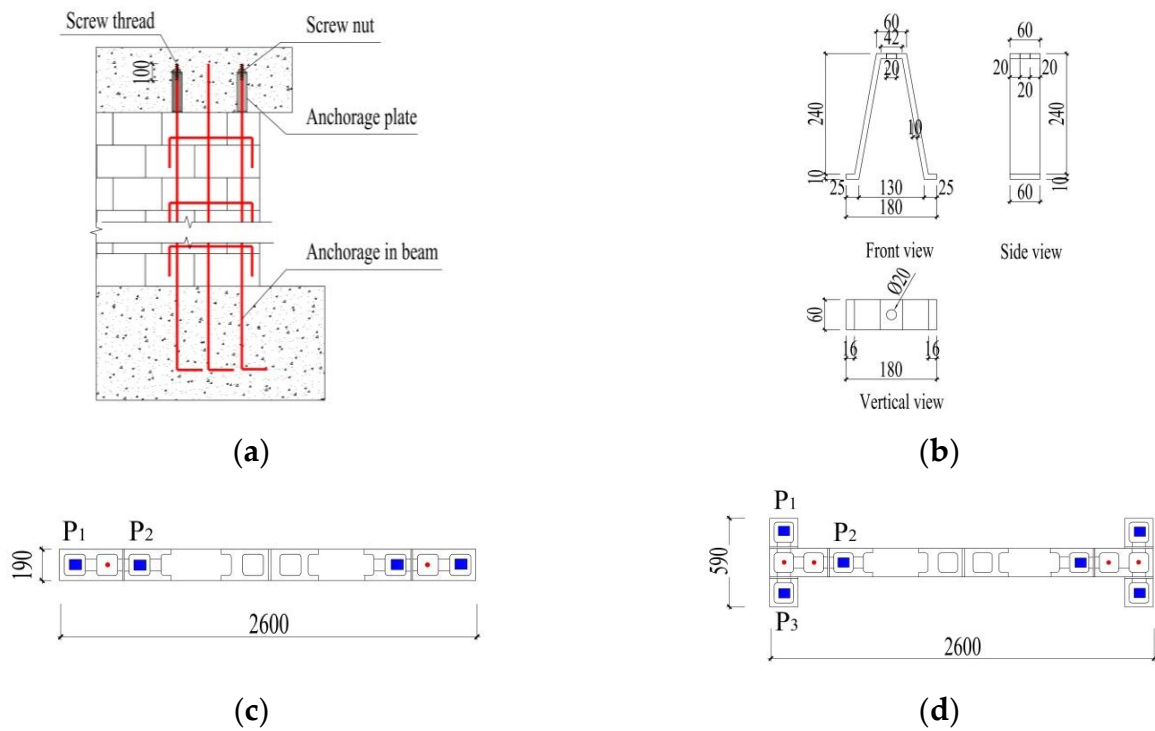


Figure 4. Details of prestressing technology: (a) schematic of prestressing technology, (b) anchorage plate (dimensions in mm), (c) prestressing zone in IMFP, and (d) prestressing zone in IMFTP.

Table 2. Detailed calculation results of tensile stress of vertical bars.

		Rectangular Section	T-Shaped Section
Prestress (MPa)		0.453	0.453
Sectional area (m ²)		0.1121	0.1181
Tensile force (kN)	P ₁	25.4	29.8
	P ₂	25.4	25.5
	P ₃	–	29.8
Tensile stress (MPa)	P ₁	126.4	193.7
	P ₂	126.4	126.9
	P ₃	–	193.7

Note: P₁, P₂, and P₃ represent the positions of prestress vertical bars, as shown in Figure 4.

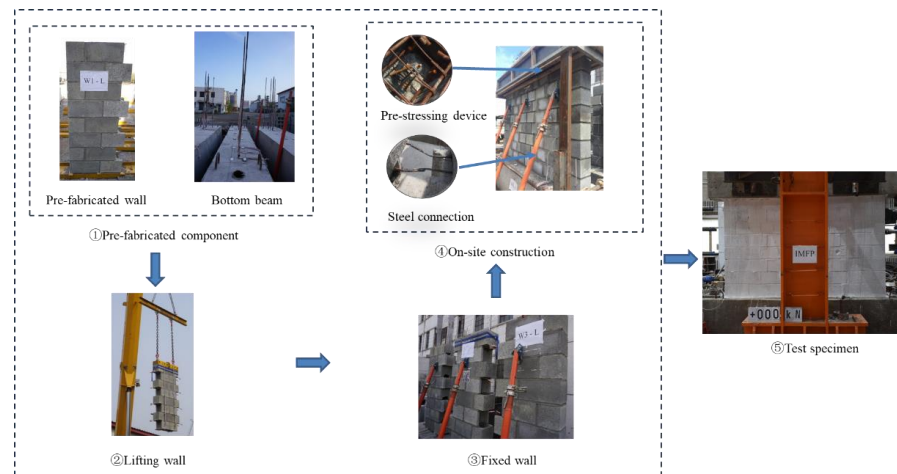


Figure 5. Process of specimen construction.

2.2. Material Properties

Five materials were used in this experiment, namely CMU, mortar, concrete, reinforcement, and AAC block. Therefore, the material properties of each material were tested due to their stress characteristics. The samples of concrete, mortar, and AAC block were made and tested to determine the compressive strength of each material according to GB 50010-2010 [38], GB/T 50129-2011 [39], and GB/T 11969-2008 [40], respectively. Moreover, five-course prisms comprising hollow CMU, mortar, and grouted concrete were tested to represent the basic masonry element, which has also been used previously in the literature [12,13]. In addition, two types of deformable bars and plain bars with different strength grades were used as vertical and horizontal reinforcements, respectively. Overall, the mechanical properties of all the materials are listed in Table 3.

Table 3. Mechanical properties of materials.

Material	Property	Testing Sample	Mean Value (MPa)	c.o.v
Concrete block prism	Compression strength		18.4	0.02
Concrete	Compression strength		29.8	0.04
Mortar	Compression strength		11.8	0.04
AAC block	Compression strength		2.3	0.04
Deformed bars	Yield strength		458.4	0.01
	Ultimate strength		648.2	0.01
Plain bars	Yield strength		226.5	0.07
	Ultimate strength		255.4	0.09

2.3. Test Setup and Measurements

The test setup is presented in Figure 6. The specimens were fixed on the floor of the laboratory using two steel bolts, and the top beam of the specimen was connected to a lateral MTS hydraulic actuator using prefabricated steel plates. Meanwhile, two couples of later support were fixed on the reaction frame supported on both sides of the top beam of the specimen, thus preventing out-of-plane displacement. Furthermore, returning to practical engineering applications, the ICMW proposed in this study was designed to be used as a force-resisting system in low-rise buildings in villages and towns, so the

compressive stress on the wall could be not large. On the other hand, the opinion that an increase in compressive stress can improve the seismic performance of wall has become a general consensus. Therefore, in order to maintain consistency with actual engineering and better analyze the influence of the prestressing technology, compressive stress was ignored and not applied to the specimen in this experiment. A similar test setup was also adopted in the studies of Chalarca B et al. [41] and Lopez A et al. [42].

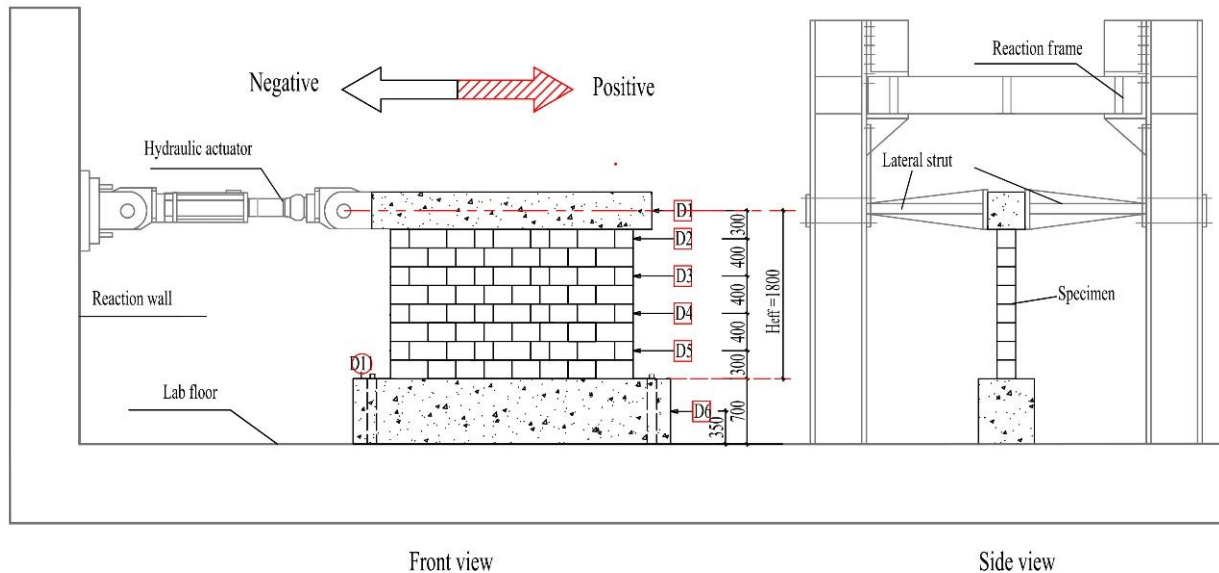


Figure 6. Test setup and schematic of instrumentation arrangements (dimensions in mm).

The measurements of the specimens are also plotted in Figure 6, marked by a red box. Linear variable differential transformers (LVDTs) can be divided into three categories according to their functionality. D1 and D6, which were placed at the center of the top and bottom beams, formed the first measurement category, and the difference between them was used as the loading control displacement. For the second category, D2–D5 were arranged on one side of the wall to obtain the deformation characteristics of the specimen. Moreover, D11 was a dial gauge used to monitor the vertical displacement of the bottom beam in real-time, which could indicate whether the bottom beam was fixed on the floor of the laboratory or not. On the other hand, strain gauges were also arranged in this experiment to monitor the stress of the steel bars. Unfortunately, it was found that many strain gauges failed during the experiment; therefore, the positions of the strain gauges are not marked in Figure 6, and a discussion on the stress of steel bars will not be carried out in this paper.

A force displacement loading mode was adopted in this experiment, and the loading protocol is plotted in Figure 7. A positive loading direction was defined as the direction when the lateral actuator applied thrust force on the specimen; accordingly, a negative positive loading direction was defined as the opposite direction, as shown in Figure 6. A force control loading protocol was adopted in the early loading stage to obtain information on the specimen in the elastic stage. Each load stage was repeated once, and the loading rates were 10 kN/min, indicating a quasi-static loading mode. When the inflection point occurred at the hysteretic curve, the force control loading protocol was replaced by the displacement control loading protocol, while the displacement cycle was repeated twice at each control displacement. In order to conduct a comparative discussion with previous research, the displacement control loading protocol used in this experiment was consistent with that used in Chi et al.'s study [18]. The damage propagation and deformation of the specimen were recorded in a timely manner during the experiment. Finally, the experiment was terminated when the lateral resistance of the specimen decreased to 60% of the maximum lateral resistance of the specimen measured in the test.

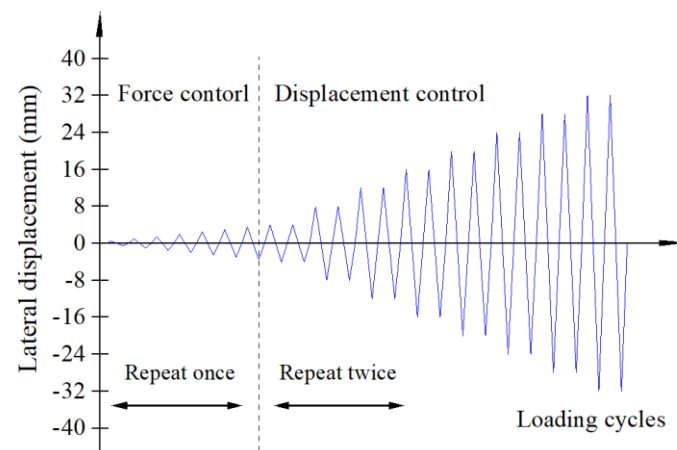


Figure 7. Loading protocol.

3. Experimental Results

3.1. Damage Propagation

Summarizing the entire process of the specimen, the damage propagation can be divided into four stages based on the development zone of cracks and changes in the load-bearing capacity of the specimen. Therefore, four damage states (DSs) were defined in this study to describe the damage propagation of the specimen. The first state (DS1) corresponded to the stage when a crack first appeared in the whole specimen, thus reflecting the weakest zone of the specimen. The second state (DS2) corresponded to the stage when a crack first appeared in the load-bearing component of the specimen, which indicated that inelastic deformation occurred in the load-bearing component. In addition, the third state (DS3) and the fourth state (DS4) were related to the lateral resistance of the specimen. DS3 corresponded to the stage of the maximum lateral resistance of the specimen, while DS4 corresponded to the stage of 85% of the maximum lateral resistance at the decrease stage of the specimen, respectively. Therefore, the damage propagations of the specimen were plotted, as shown in Figure 8. The blue and red lines represent the propagation of cracks in the positive and negative directions, respectively.

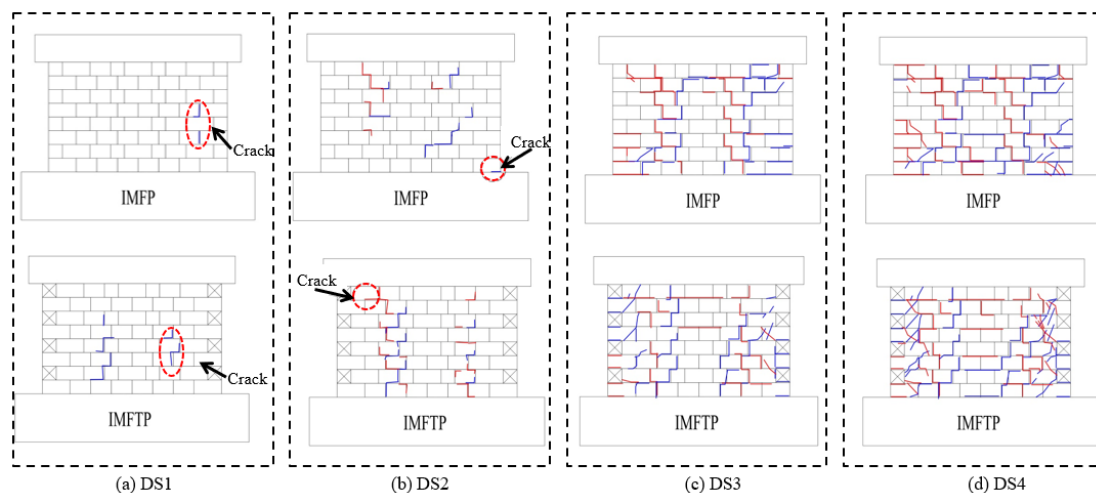


Figure 8. Crack propagation of specimens IMFP and IMFTP.

Figure 8 clearly indicates that stepped cracks first occurred in the mortar layers around the weak planes of the specimen. This phenomenon was consistent with the previous assumptions made about the functional zone of the specimen. As there was an increase in the loading force, cracks around the weak plane developed fully and occurred at the load-bearing component of the specimen, indicating that the specimen reached DS2. After that,

with an increase in the loading displacement, weak planes were squeezed by functional components on both sides; hence, the mortar layers around the weak planes were split, and gaps appeared between the load-bearing component and in-fill component. Cracks were gradually observed at the top or bottom zone of the load-bearing component and in-fill component during the process of the specimen from DS2 to DS3, as shown in Figure 9. However, owing to the increase in the gaps, the cracks in the in-fill component were observed to no longer increase with the increase in the displacement, which demonstrated that the in-fill component did not participate in the later loading process of the whole specimen. Finally, damage to the load-bearing component gradually accumulated, and the in-fill component gradually withdrew from the specimen, leading to a decrease in the load-bearing capacity of the specimen.



Figure 9. Damage state of specimens: (a) specimen IMFP; (b) specimen IMFTP.

3.2. Failure Pattern

The final failure patterns of the specimens are shown in Figure 10. The similarity of the failure patterns of the two specimens was that the weak planes were seriously damaged, while the in-fill component still maintained in-plane integrity with few cracks. The load-bearing components were also seriously damaged; however, the failure pattern of each specimen was different according to the section type. For specimen IMFP with a rectangular section, the cracks were concentrated at the top and bottom zones, and bottom masonry face spalling occurred. However, for specimen IMFTP with a T-shaped section, the cracks were distributed uniformly, and cross-cracks occurred at the middle of the web plane of the load-bearing component, while only horizontal cracks were observed at the flange plane. Based on the typical failure characteristics of masonry walls in previously conducted studies in the literature [13–15], it could be concluded that bending failure and shear failure occurred in specimens IMFP and IMFTP, respectively.



Figure 10. End states of specimens: (a) specimen IMFP; (b) specimen IMFTP.

3.3. Hysteretic Curves and Characteristic Points

Based on the cyclic test results, the load–displacement hysteretic curves of the two specimens were plotted, as shown in Figure 11. The envelop curves and four damage state characteristic points are also depicted in Figure 11. The drift ratio (DR) was defined as the ratio of the top displacement and loading height of the specimen for subsequent analysis, while the loading height was calculated as 1800 mm, as shown in Figure 6. Therefore, a significant and nearly symmetrical pinching effect was observed in the load–displacement curves of the two specimens. The appearance of the overall load–displacement curves was S-shaped, and an obvious slip phenomenon was observed in the unloading stage of each loading loop. The lateral resistance of the specimen increased rapidly at the prepeak stage of the load–displacement curves and decreased gradually at the postpeak stage. Moreover, the characteristic point information corresponding to different damage states is listed in Table 4 and marked in Figure 11. The existence of flanges increased the maximum lateral resistance of specimen IMFTP by 32% compared to specimen IMFP, and the positive lateral resistance of the two specimens was higher than the negative lateral resistance owing to damage accumulation. Therefore, a detailed discussion of the seismic performance of the two specimens is carried out in the next section, and the relevant data of the comparison of specimens IMF and IMFT introduced by Chi et al. [18] were also adopted to assess the influence of the prestressing technology on the specimen.

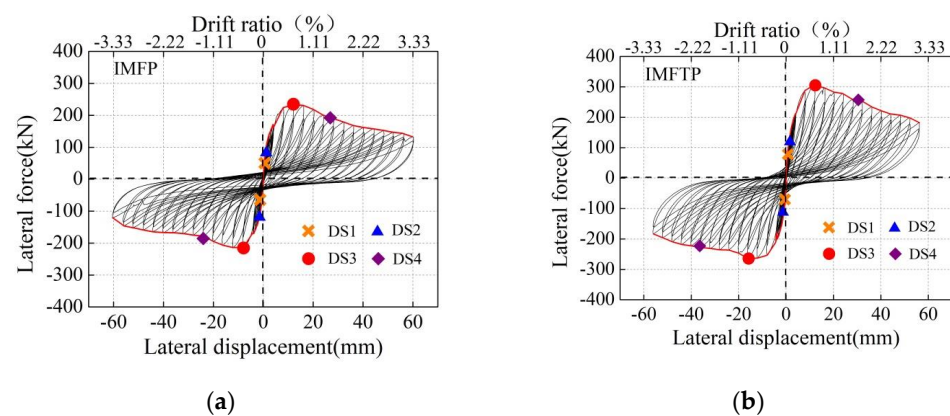


Figure 11. Hysteretic curves of specimens: (a) specimen IMFP; (b) specimen IMFTP.

Table 4. Damage state characteristic points.

Specimen	Direction	DS1		DS2		DS3		DS4	
		Q (kN)	DR (%)						
IMFP	+	+60	+0.03	+90	+0.06	+232	+0.67	+197	+1.39
	−	−70	−0.04	−130	−0.11	−214	−0.44	−182	−1.22
IMFTP	+	+70	+0.03	+140	+0.09	+306	+0.67	+260	+1.56
	−	−70	−0.03	−100	−0.04	−264	−0.89	−225	−2.11

4. Parameter Discussion

4.1. Influence on Hysteretic Curves

Hysteresis curves are the basis for analyzing the seismic performance of structures; therefore, a comparison of the hysteresis curves for the specimens with and without prestressing technology is plotted in Figure 12. As shown in Figure 12, an obvious pinching effect was observed at both comparisons of the specimens, and the overall appearance of the hysteresis curves of the specimens with and without prestressing technology was similar. Moreover, Figure 12 shows that the influence of the prestressing technology was marginal for IMFTP, while it became more important for IMFP. This phenomenon reflected

that there was a correlation between the improvement in the prestressing technology on the hysteresis curve of the specimens and the failure mode of the specimens. The shear failure of the specimens was mainly related to their shear strength, while the shear strength was commonly considered to be related to the horizontal steel bars, the compressive strength of the grouted masonry, and the compressive stress. In this study, the in-site vertical bars of the specimens were used to apply prestress, and this method can be regarded to improve the compressive strength of grouted masonry. However, the same configuration of the horizontal steel bars in specimens IMFTP and IMFT may be the main reason for their similar bearing capacity; that is, the shear failure of the specimens was caused by the insufficient configuration of shear reinforcement. A similar conclusion was also found in Hassanili et al. [26] and Laursen and Ingham [31]. Furthermore, the damage state characteristic points of the comparison specimens in the positive direction are listed in Table 5, and the normalized skeleton curve is plotted at Figure 13. The normalized lateral force and displacement were chosen as the vertical and horizontal axes. For normalization, the lateral force (V) and displacement (Δ) of each loading cycle of the specimens were divided by the max lateral force (V_{max}) and corresponding displacement (Δ_{max}), respectively. It should be noted that DS1 and DS2 of the specimens were related to the initial cracking of the specimens, directly determined by the tensile stress around the weak plane and fully grouted CMWs, respectively. In this study, the mortar strength remained consistent at the above locations of the comparison specimens, indicating that the tensile stress around the weak plane was greater than that in the fully grouted CMWs. The improvement in the mortar strength may have delayed the occurrence of DS1 in the specimens. Moreover, as shown in Figure 13, the upward trend of the normalized skeleton curve of the comparison specimens was observed to be similar before the specimens reached DS3. After that, the downward trend of the specimen with prestressing technology was lower than the specimen without, especially for the specimens with a T-shaped section. This indicates that the prestressing technology improved the seismic performance of the specimen after DS3, and this was also related to the ductility of the specimen, which will be discussed later. In this regard, a greater amount of experimental data is needed to validate this conclusion.

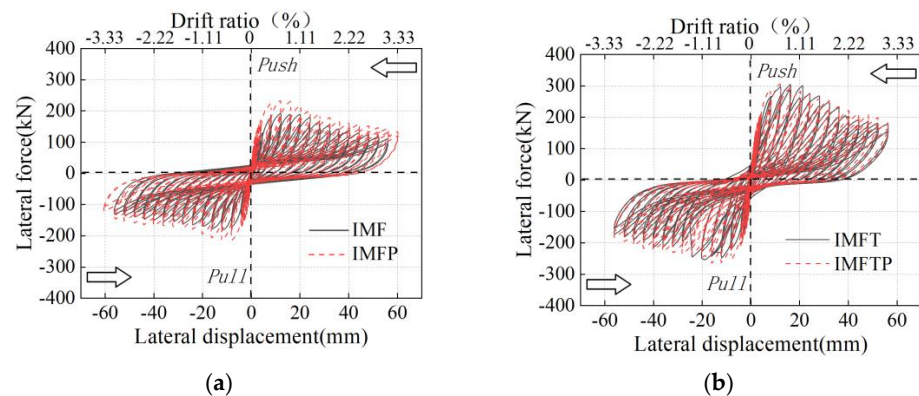


Figure 12. Comparison of hysteretic curves of specimens [18]: (a) specimen with rectangular section; (b) specimen with T-shaped section.

Table 5. Comparison of damage state characteristic points of specimens.

Specimen	DS1		DS2		DS3		DS4	
	Q (kN)	DR (%)						
IMFP	+60	+0.03	+90	+0.06	+232	+0.67	+197	+1.39
IMFTP	+70	+0.03	+140	+0.09	+306	+0.67	+260	+1.56
IMF [18]	+60	+0.06	+70	+0.07	+191	+0.66	+162	+1.56
IMFT [18]	+60	+0.03	+80	+0.06	+304	+0.88	+258	+1.66

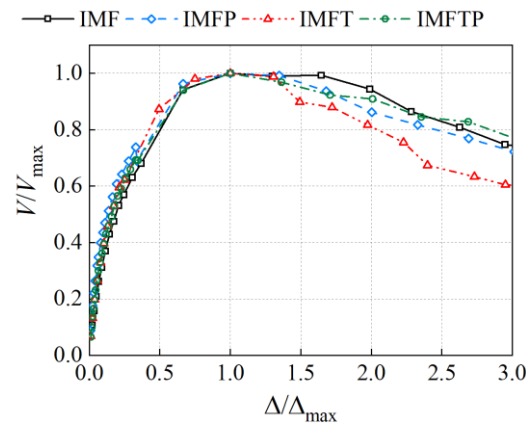


Figure 13. Comparison of normalized skeleton curve of specimens [18].

4.2. Influence on Stiffness Degradation

Stiffness is an important index of the seismic performance of specimens that can be used to restore the model and nonlinear analysis of the specimens. In this study, the secant stiffness K_{si} was calculated from the slope of the line that joins the positive and negative peaks in each loading cycle [43,44], and the initial stiffness was determined as K_{s0} of the first loading cycle. Table 6 presents the values of that which responded to each damage state of the specimen, and K_{si}/K_{s0} at each damage state was also calculated and recorded for the normalization analysis. To clearly compare the stiffness degradation of the specimens, the stiffness of the specimens before they reached DS3 was analyzed, and the value of K_{si} of the specimens with respect to DR is plotted in Figure 14a, while the stiffness of the specimens at a different DSs is plotted in Figure 14b. Moreover, to analyze the influence of the prestressing technology, the data of specimens IMF and IMFT related to different damage states were also adopted and are listed in Table 6.

Table 6. Comparison of stiffness of specimen.

Specimen	Initial	DS1		DS2		DS3		DS4	
	K_{s0} (kN/mm)	K_{s1} (kN/mm)	$\frac{K_{s1}}{K_{s0}}$	K_{s2} (kN/mm)	$\frac{K_{s2}}{K_{s0}}$	K_{s3} (kN/mm)	$\frac{K_{s3}}{K_{s0}}$	K_{s4} (kN/mm)	$\frac{K_{s4}}{K_{s0}}$
IMFP	171.9	118.5	0.69	94.9	0.55	18.5	0.11	6.5	0.04
IMFTP	216.4	152.5	0.70	89.0	0.41	23.7	0.11	8.8	0.04
IMF [18]	85.2	56.8	0.67	50.9	0.60	15.4	0.18	5.9	0.07
IMFT [18]	127.0	94.5	0.69	85.3	0.55	16.9	0.13	7.2	0.06

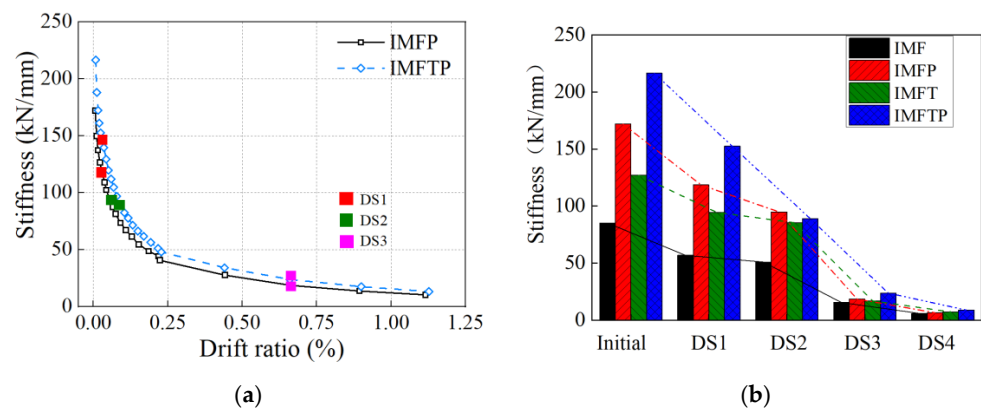


Figure 14. Comparison of stiffness degradation of the specimens [18]: (a) stiffness degradation of the specimens with respect to drift ratio; (b) stiffness of specimen at different DSs.

Table 5 and Figure 14 clearly indicate that the stiffness of the specimens decreased gradually with an increase in the drift ratio. The initial stiffness of specimen IMFTP increased by 26% compared to that of specimen IMFP. The values of K_{si}/K_{s0} at four damage states showed that the stiffness degradation trend of specimens IMFP and IMFTP was similar, while the stiffness degradation of specimen IMFP was faster than that of specimen IMFTP from DS2 to DS3. Moreover, owing to the prestressing technology, the initial stiffness of the specimens with a rectangular section and T-shaped section also increased by 101% and 70%, respectively. For further research, the normalized stiffness degradation of the comparison specimens with respect to the drift ratio is plotted in Figure 15. As shown in Figure 15, the rate of normalized stiffness degradation of the specimen with prestressing technology was higher than that of the specimen without prestressing technology. The stiffness of specimens IMFP and IMFTP was higher than that of specimens IMF and IMFT at DS2, while the stiffness of specimens IMFP and IMFTP was like that of specimens IMF and IMFT at DS3 and DS4, indicating that the influence of the prestressing technology on the stiffness of the specimen gradually weakened. In this study, in situ vertical reinforcement was used as a prestressed reinforcement, and the application of the prestressing technology was completed during the specimen construction process, resulting in an increase in the initial stiffness of the specimen. When the specimen was subjected to lateral force, those reinforcements participated in the mechanical mechanism of the specimen as a traditional reinforcement; therefore, the influence of the prestressing technology on the specimen was weakened with the increase in the drift ratio. However, further research is necessary for the purpose of verification.

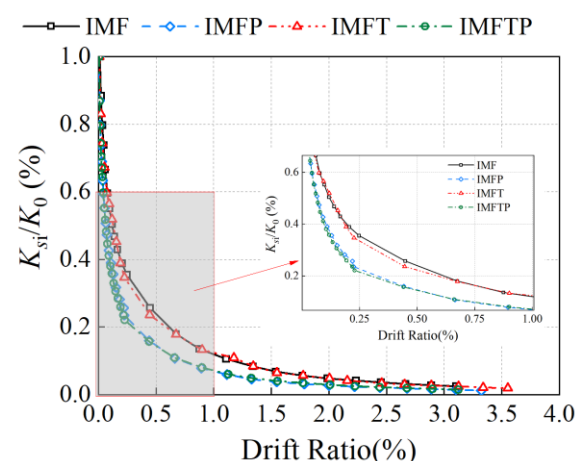


Figure 15. Comparison of the normalized stiffness degradation of specimens [18] with respect to DR.

4.3. Influence on Displacement Ductility

The displacement ductility can be used to evaluate the deformation capacity of specimens subjected to seismic load, thus avoiding brittle failure. In this study, the displacement ductility was defined as the ratio of the ultimate displacement (Δ_u) to the yield displacement (Δ_y). The ultimate displacement was chosen as the corresponding displacement of DS4, and the yield displacement was calculated using the energy equivalence method [45,46], as shown in Figure 16. Considering the influence of damage accumulation caused by the cyclic loading protocol, the analysis of the displacement ductility was calculated using data only from the positive direction. Hence, the calculation results of the two specimens used in this study and the comparison specimens in Chi et al.'s study [18] are listed in Table 7.

In general, the displacement ductility of the specimen was related to the failure mode, where the displacement ductility of the specimen with a flexural failure mode was better than that of the specimens with a shear failure mode [4,44]. Based on the failure pattern shown in Figure 10, the flexural failure mode occurred in the load-bearing component of specimen IMFP, while the shear failure mode occurred in that of specimen IMFTP. It could be found that the displacement ductility coefficients of the four specimens were in the

range of 4.03–4.66. The displacement ductility coefficients of specimens IMFP and IMFTP were relatively close. Moreover, the displacement ductility of specimens IMFP and IMFTP increased by 6% and 16% compared to that of specimens IMF and IMFT, respectively. This showed that the prestressing technology overall improved the displacement ductility of the specimen, while the influence law on the displacement ductility of specimens with a different failure mode still needs to be further studied. Also, it is necessary to perform further research for the purpose of verification.

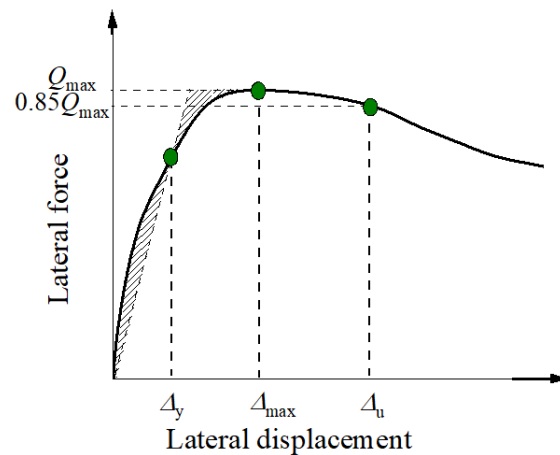


Figure 16. Method to calculate displacement ductility.

Table 7. Displacement ductility results.

Specimen	Yield State			Ultimate State			Ductility μ
	Q (kN)	Δ_y (mm)	DR (%)	Q (kN)	Δ_u (mm)	DR (%)	
IMFP	+182	+5.4	+0.30	+197	+25.0	+1.39	4.63
IMFTP	+248	+6.0	+0.33	+260	+28.0	+1.56	4.66
IMF [18]	+157	+6.4	+0.35	+162	+28.0	+1.55	4.38
IMFT [18]	+254	+7.4	+0.41	+259	+29.8	+1.65	4.03

4.4. Influence on Energy Dissipation and Equivalent Viscous Damping

In general, the energy dissipation was calculated by the area enclosed by a single cycle of the load–displacement curve, as depicted by blue dashed lines in Figure 17, and the equivalent viscous damping can be calculated using formula $\zeta_{eq} = \frac{1}{2\pi} \frac{E_d}{E_s}$, where E_s is the strain energy at the maximum lateral force of the same cycle, which is depicted by black lines in Figure 17 [47]. Therefore, the energy dissipation and equivalent viscous damping of two specimens were plotted, as shown in Figure 18. Figure 18 clearly indicates that the energy dissipation of the two specimens increased rapidly after a DR of 2.0%, while that of specimen IMFTP tended to remain constant after a DR of 2.0%. Additionally, the equivalent viscous damping ζ_{eq} initially decreased, followed by a slight increase, and then a constant value was reached after a DR of 1.5% was achieved. Specimen IMFP finally converged at 8%, while specimen IMFTP finally converged at 14%, respectively.

Moreover, analyses of the energy dissipation and equivalent viscous damping of the comparison specimens IMF and IMFT before the specimens reached DS4 were carried out in this study; the comparison results are drawn in Figure 19. The analyses showed that the influence of the prestressing technology on the energy dissipation and equivalent viscous damping of the specimens decreased with an increase in DR. The energy dissipation of specimens IMFP and IMFTP was higher than that of specimens IMF and IMFT, while the ζ_{eq} of specimens IMFP and IMFTP was lower than that of specimens IMF and IMFT before a DR of 0.25% was achieved. This indicated that the equivalent viscous damping of the

specimen with the prestressing technology needed to be considered specifically in the structural design.

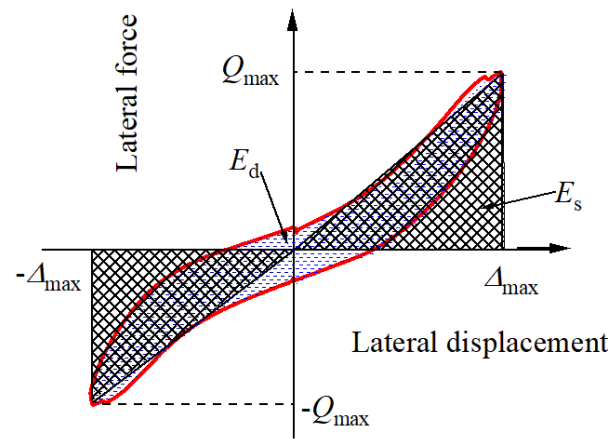


Figure 17. Definition of energy dissipation and equivalent viscous damping.

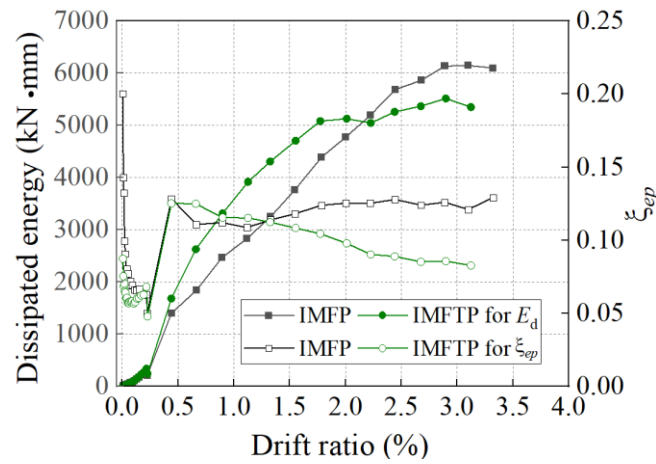


Figure 18. The energy dissipation and equivalent viscous damping of specimens with respect to DR.

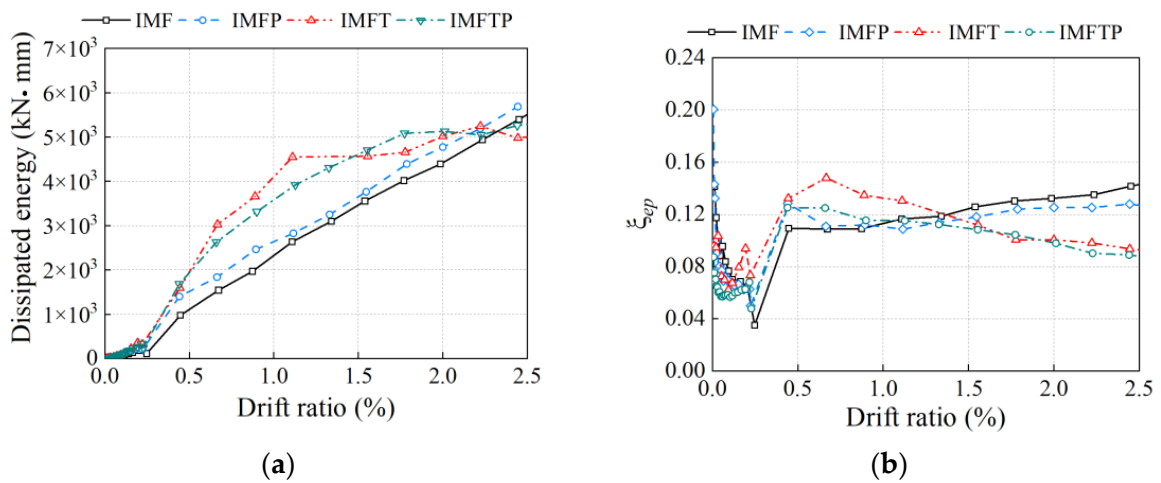


Figure 19. Comparison results of the specimens [18]: (a) energy dissipation; (b) equivalent viscous damping.

4.5. Influence on Damage Propagation and Deformation

The crack propagation and deformation of specimens IMFP and IMFTP and the comparison specimens IMF and IMFT at the same DR are shown in Figures 20 and 21, respectively. As mentioned before, flexural failure was observed at the load-bearing component of IMFP, while shear failure was observed at the load-bearing component of IMFTP. Therefore, a similar failure pattern was observed in the specimens with a similar configuration of the load-bearing component, indicating that the prestressing technology did not change the failure pattern of the specimens. However, fewer and finer cracks were observed in the specimen with the prestressing technology, which showed that the prestressing technology improved the damage propagation of the specimen. With regard to the deformation of the specimens, IMFP-B represented that the load-bearing component of IMFP was away from the loading lateral actuator. The deformation of the specimens at different DRs was chosen corresponding to the specimens in different damage states. It could be observed that the deformation of the specimens could basically remain straight at a DR of 0.22%, while an inflection point occurred at a height of 1100 mm in specimens IMFP and IMFTP at a DR of 0.89%. As shown in Figure 21a,b, the deformation of specimen IMFP-B was slightly lower than that of the comparison specimen, while the deformation of specimen IMFTP-B was larger than that of specimen IMFT-B at a DR of +0.89%. This reflected a higher compressive stress and deformation in the bottom zone of IMFTP-B than in that of specimen IMFT. This phenomenon was related to the prestressing technology and failure pattern of the specimen. The prestressing technology could improve the specimen cracking situation caused by insufficient tensile strength; however, it could have had an impact on the compressive failure of the specimens due to having a smaller margin to develop new compressive strains. With regard to specimen IMFTP, the zone of the specimen at a height between 300 mm and 1100 mm was in the shear-compression zone, which may have resulted in larger deformation due to damage propagation. Therefore, it could be concluded that the prestressing technology had a positive influence on the damage propagation and deformation of the specimen before DS3; however, additional research on the deformation of the compression zone of specimens caused by a high compressive stress is essential, which will hopefully provide a reference for the value of prestressing in future structural design.

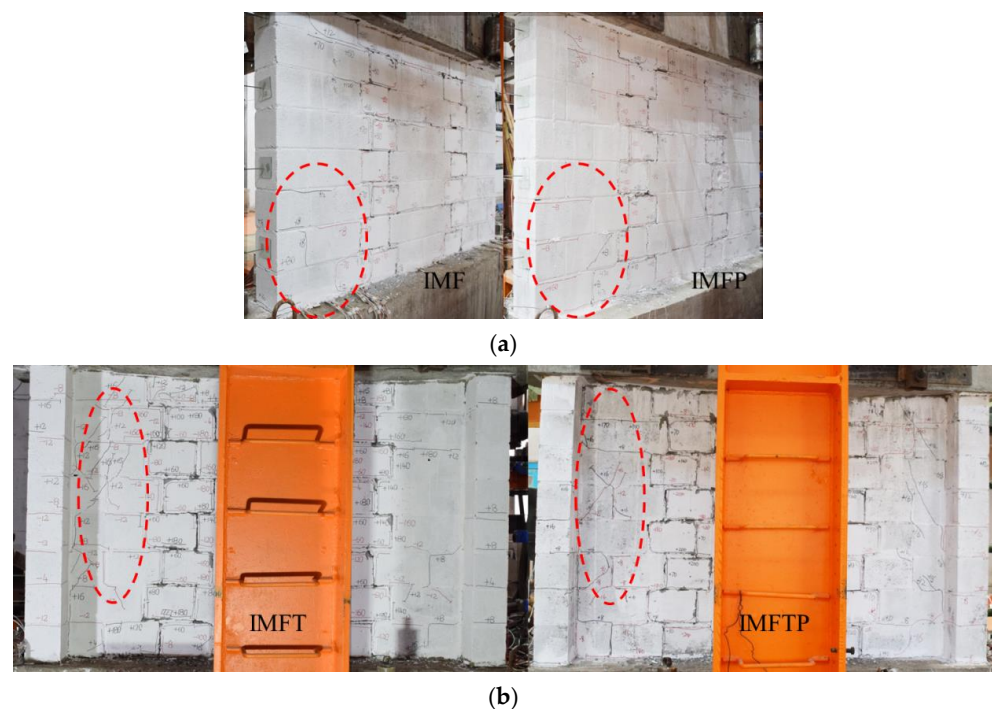


Figure 20. Comparison of crack propagation of specimens [18]: (a) DR = 0.67% and (b) DR = 0.89%.

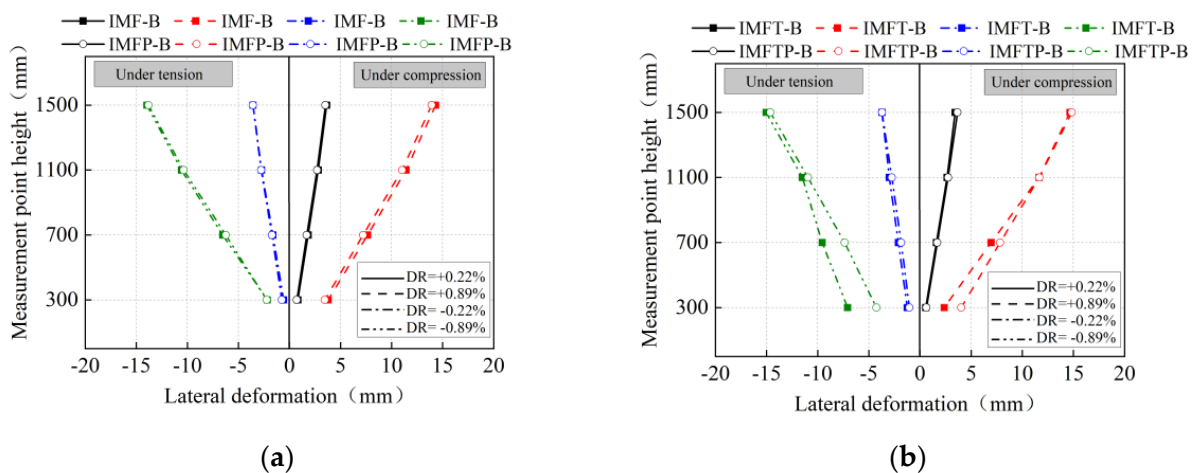


Figure 21. Comparison results of deformation of all specimens [18] along wall height: (a) specimen with rectangular section; (b) specimen with T-shaped section.

5. Conclusions

In this study, we proposed an innovative ICMW structural system with prestressing technology. Two specimens with different section types were constructed and tested under reverse cyclic tests. Four damage states related to the crack and load resistance of the specimens were defined, and the seismic performance of the specimens was evaluated, consisting of crack propagation, stiffness degradation, displacement ductility, and equivalent viscous damping based on the experiment results from this study and previous research. The main findings and conclusions of this study are summarized as follows:

- (1) Cracks were initially observed at the mortar layers around the weak planes of the specimens and subsequently in the load-bearing component. The gap between the load-bearing component and in-fill component appeared with an increase in the drift ratio, which protected the in-fill component at a larger drift ratio. At last, the specimen with a rectangular section was observed to be in the flexural failure mode, while the specimen with a T-shaped section was observed to be in the shear failure mode, respectively. The prestressing technology had a positive influence on the crack propagation and deformation of the specimen before it reached lateral resistance; however, it is necessary to conduct additional research on the relationship between the deformation of specimens with prestressing technology under a larger drift ratio and different failure patterns.
- (2) The existence of flanges and the prestressing technology improved the initial stiffness of the specimen, while the degradation rate of the specimen with the prestressing technology was higher than that of the specimen without. The influence of the prestressing technology on the stiffness of the specimen was gradually weakened with an increase in the drift ratio. The displacement ductility coefficients of specimens IMFP and IMFTP were 4.63 and 4.66, respectively. Although the prestressing technology advanced the yield displacement of the specimen, the ductility of specimens IMFP and IMFTP increased by 6 and 16% in comparison with that of the reference specimens in previous research, which indicated that the prestressing technology had a positive influence on the displacement ductility of the specimen.
- (3) The energy dissipation of the two specimens increased rapidly after a DR of 2.0% was achieved, while that of specimen IMFTP tended to remain constant after a DR of 2.0% was obtained. The equivalent viscous damping initially decreased, followed by a slight increase, and then a constant value was reached after a DR of 1.5% was achieved. Specimen IMFP finally converged at 8%, while specimen IMFTP finally converged at 14%. The influence of the prestressing technology on the energy dissipation and equivalent viscous damping of the specimens decreased with an increase in the drift ratio. However, the equivalent viscous damping of the specimen with the prestressing

technology was lower than that of the specimen without before a drift ratio of 0.25% was achieved, which indicates that the equivalent viscous damping of specimens with prestressing technology needs to be especially considered in structural design.

Overall, the prestressing technology proposed in this study has the potential to become a method for improving the damage propagation and seismic performance of ICMW, and the advantages of ICMW, such as the timely separation of the in-fill component to protect its integrity, are retained. However, many factors, such as construction method optimization, prestress loss, and the relationship between the material strength and failure pattern of ICMW, have not been explored. Also, more detailed numerical models need to be provided to study the mechanics mechanism and seismic performance of ICMW. Therefore, additional experiments and numerical investigations are necessary to complement and provide proper design guidelines for ICMW systems.

Author Contributions: B.C.: methodology, investigation, resources, and data curation; Y.Q.: formal analysis, visualization, and writing—review and editing; F.W.: conceptualization, writing—review and editing, supervision, and funding acquisition. X.Y.: data curation and investigation. All authors have read and agreed to the published version of the manuscript.

Funding: This work was funded by the National Natural Science Foundation of China (No: 52208190) and National Key R&D Plan-China (grant number 2016YFC0701502-3).

Data Availability Statement: Data will be made available on request.

Acknowledgments: The authors gratefully acknowledge the technical support provided by Harbin Dacheng Green Building Technology Developing Co., Ltd., and financial support provided by the National Natural Science Foundation of China (No: 52208190) and National Key R&D Plan-China (grant number 2016YFC0701502-3). The authors would also like to thank Zhiming Zhang, who helped in conducting the experimental program.

Conflicts of Interest: The authors declare no conflicts of interest.

References

1. Zhao, B.; Taucer, F.; Rossetto, T. Field investigation on the performance of building structures during the 12 May 2008 Wenchuan earthquake in China. *Eng. Struct.* **2009**, *31*, 1707–1723.
2. Yön, B. Identification of failure mechanisms in existing unreinforced masonry buildings in rural areas after April 4, 2019 earthquake in Turkey. *J. Build. Eng.* **2021**, *43*, 102586.
3. Deng, M.; Zhang, W.; Li, N. In-plane cyclic loading tests of concrete hollow block masonry walls retrofitted with high ductile fiber-reinforced concrete. *Constr. Build. Mater.* **2020**, *238*, 117758.
4. El-Dakhkhni, W.; Ashour, A. Seismic response of reinforced-concrete masonry shear-wall components and systems: State of the art. *J. Struct. Eng.* **2017**, *43*, 03117001. [[CrossRef](#)]
5. Mohamad, G.; Lourenço, P.B.; Roman, H.R. Mechanics of hollow concrete block masonry prisms under compression: Review and prospects. *Cem. Concr. Compos.* **2007**, *29*, 181–192. [[CrossRef](#)]
6. Janaraj, T.; Dhanasekar, M. Effectiveness of two forms of grouted confinement methods to hollow concrete masonry panels. *J. Mater. Civ. Eng.* **2015**, *27*, 04015038. [[CrossRef](#)]
7. Dhanasekar, M.; Shrive, N.G. Strength and deformation of confined and unconfined grouted concrete masonry. *ACI Struct. J.* **2002**, *99*, 819–826.
8. Bolhassani, M.; Hamid, A.A.; Johnson, C.; Moon, F.L.; Schultz, A.E. New design detail to enhance the seismic performance of ordinary reinforced partially grouted masonry structure. *J. Struct. Eng.* **2016**, *142*, 04016142. [[CrossRef](#)]
9. Ramírez, P.; Sandoval, C.; Almazán, J.L. Experimental study on in-plane cyclic response of partially grouted reinforced concrete masonry shear walls. *Eng. Struct.* **2016**, *126*, 598–617. [[CrossRef](#)]
10. Zhang, Z.; Murcia-Delso, J.; Sandoval, C.; Araya-Letelier, G.; Wang, F. In-plane shear strength and damage fragility functions for partially-grouted reinforced masonry walls with bond-beam reinforcement. *Eng. Struct.* **2021**, *242*, 112569.
11. Shedid, M.T.; El-Dakhkhni, W.W.; Drysdale, R.G. Seismic performance parameters of reinforced concrete-block shear wall construction. *J. Perform. Constr. Facil.* **2010**, *24*, 4–18.
12. Voon, K.C.; Ingham, J.M. Experimental in-plane shear strength investigation of reinforced concrete masonry walls. *J. Struct. Eng.* **2006**, *132*, 400–408.
13. Zhang, Z.; Wang, F.; Chi, B. Seismic performance of shear-critical prefabricated reinforced masonry shear walls with innovative vertical joint connections. *Eng. Struct.* **2020**, *219*, 110958.

14. Eldin, H.M.S.; Galal, K. Effect of reinforcement anchorage end detail and spacing on seismic performance of masonry shear walls. *Eng. Struct.* **2018**, *157*, 268–279. [[CrossRef](#)]
15. Eldin, H.M.S.; Ashour, A.; Galal, K. Seismic performance parameters of fully grouted reinforced masonry squat shear walls. *Eng. Struct.* **2019**, *187*, 518–527. [[CrossRef](#)]
16. Silva, L.M.; Vasconcelos, G.; Lourenço, P.B. Innovative systems for earthquake-resistant masonry infill walls: Characterization of materials and masonry assemblages. *J. Build. Eng.* **2021**, *39*, 102195. [[CrossRef](#)]
17. Kasapgil, S.M.; Binici, B.; Canbay, E. Seismic behavior of AAC infill walls insulated with cementitious lightweight panels in reinforced concrete frames. *Eng. Struct.* **2021**, *248*, 113215.
18. Chi, B.; Yang, X.; Wang, F.; Zhang, Z.; Quan, Y. Experimental investigation of effect of section configuration on seismic performance of an innovative integrated concrete masonry wall system. *Eng. Struct.* **2020**, *206*, 110163.
19. Markulak, D.; Dokšanović, T.; Radić, I.; Miličević, I. Structurally and environmentally favorable masonry units for infilled frames. *Eng. Struct.* **2018**, *175*, 753–764.
20. Torres, B.; Ivorra, S.; Baeza, F.J.; Estevan, L.; Varona, B. Textile reinforced mortars (TRM) for repairing and retrofitting masonry walls subjected to in-plane cyclic loads. An experimental approach. *Eng. Struct.* **2021**, *231*, 111742. [[CrossRef](#)]
21. Gao, Q.; Xiao, J.; Shen, J.; Hou, Y.; Guo, J. Properties of super-thin layer mortar with recycled brick fines for sintered perforated block masonry. *Case Stud. Constr. Mater.* **2023**, *18*, e02015.
22. Hasnat, A.; Das, T.; Ahsan, R.; Alam, A.T.; Ahmed, H. In-plane cyclic response of unreinforced masonry walls retrofitted with ferrocement. *Case Stud. Constr. Mater.* **2022**, *17*, e01630.
23. Qiao, Q.; Ding, R.; Liu, W.; Cao, W. Experimental study on seismic behavior of masonry walls retrofitted with steel-member and high-performance polymer mortar. *J. Build. Eng.* **2023**, *75*, 106940.
24. Xin, R.; Ma, P. Experimental investigation on the in-plane seismic performance of damaged masonry walls repaired with grout-injected ferrocement overlay. *Constr. Build. Mater.* **2021**, *282*, 122565. [[CrossRef](#)]
25. Kohail, M.; Elshafie, H.; Rashad, A.; Okail, H. Behavior of post-tensioned dry-stack interlocking masonry shear walls under cyclic in-plane loading. *Constr. Build. Mater.* **2018**, *196*, 539–554. [[CrossRef](#)]
26. Hassanli, R.; ElGawady, M.A.; Mills, J.E. Experimental investigation of in-plane cyclic response of unbonded posttensioned masonry walls. *J. Struct. Eng.* **2016**, *142*, 04015171-1. [[CrossRef](#)]
27. Rosenboom, O.A.; Kowalsky, M.J. Reversed in-plane cyclic behavior of posttensioned clay brick masonry walls. *J. Struct. Eng.* **2004**, *130*, 787–798. [[CrossRef](#)]
28. Wight, G.D.; Ingham, J.M.; Wilton, A.R. Innovative seismic design of a post-tensioned concrete masonry house. *Can. J. Civ. Eng.* **2007**, *34*, 1393–1402. [[CrossRef](#)]
29. Hassanli, R. In-plane flexural response of self-centering masonry walls (SMWs). *Arch. Civ. Mech. Eng.* **2021**, *21*, 63.
30. Kalliontzis, D.; Schultz, A.E. Characterizing the in-plane rocking response of masonry walls with unbonded posttensioning. *J. Struct. Eng.* **2017**, *143*, 04017110. [[CrossRef](#)]
31. Laursen, P.T.; Ingham, J.M. Structural testing of single-storey post-tensioned concrete masonry walls. *TMS J.* **2001**, *19*, 69–82.
32. Guo, Z.; Zheng, S.; Xu, Z.; Sun, W. Experimental study on seismic performance of ungrouted confined concrete masonry walls with unbonded tendons. *Int. J. Civ. Eng.* **2019**, *17*, 333–346.
33. Yassin, A.; Wiebe, L.; Ezzeldin, M. Seismic design and performance evaluation of controlled rocking masonry shear walls without posttensioning. *J. Struct. Eng.* **2022**, *148*, 04022059. [[CrossRef](#)]
34. Yassin, A.; Ezzeldin, M.; Wiebe, L. Experimental assessment of resilient controlled rocking masonry walls with replaceable energy dissipation. *J. Struct. Eng.* **2023**, *149*, 04022260. [[CrossRef](#)]
35. East, M.; Yassin, A.; Ezzeldin, M.; Wiebe, L. Development of controlled rocking masonry walls with energy dissipation accessible in a steel base. *J. Struct. Eng.* **2023**, *149*, 04023032. [[CrossRef](#)]
36. Kalliontzis, D.; Schultz, A.E.; Sritharan, S. Unbonded post-tensioned structural masonry wall with rubber interface for limited-damage systems. *J. Struct. Eng.* **2022**, *148*, 04021223. [[CrossRef](#)]
37. GB 50003-2011; Code for Design of Masonry Structures. China Architecture and Building Press: Beijing, China, 2011. (In Chinese)
38. GB 50010-2010; Code for Design of Concrete Structures. China Architecture and Building Press: Beijing, China, 2010. (In Chinese)
39. GB/T 50129-2011; Standard for Test Method of Basic Mechanics Properties of Masonry. China Architecture and Building Press: Beijing, China, 2011. (In Chinese)
40. GB/T 11969-2008; Test Methods of Autoclaved Aerated Concrete. China Quality Inspection Press: Beijing, China, 2008. (In Chinese)
41. Chalarca, B.; Bedoya-Ruiz, D.; Herrera, J.P. Experimental behavior and seismic performance assessment of Unbonded Post-tensioned Precast Concrete Walls for low-rise buildings. *Eng. Struct.* **2023**, *289*, 116251. [[CrossRef](#)]
42. Lopez, A.; Bazaez, R.; Leiva, G.; Loyola, R.; Gómez, M. Experimental study of in-plane flexural behavior of screen-grid insulated concrete form rectangular and T-shaped walls. *Eng. Struct.* **2021**, *247*, 113128.
43. Zhou, Y.; Chen, Z.; Zhong, G. Investigation on the seismic performance of the masonry infill wall with damping layer joint. *Eng. Struct.* **2023**, *285*, 115979. [[CrossRef](#)]
44. Haach, V.G.; Vasconcelos, G.; Lourenço, P.B. Experimental analysis of reinforced concrete block masonry walls subjected to in-plane cyclic loading. *J. Struct. Eng.* **2010**, *136*, 452–462. [[CrossRef](#)]

45. Ke, X.-J.; Qin, Y.; Chen, S.-J.; Li, N. Seismic performance and shear lag effect of T-shaped steel plate reinforced concrete composite shear wall. *Eng. Struct.* **2023**, *289*, 116303. [[CrossRef](#)]
46. Wang, L.; Tang, Z.-Y.; Li, Y.; Qian, K. Seismic behavior of masonry-infilled precast concrete frames considering effects of opening. *Constr. Build. Mater.* **2019**, *211*, 756–770. [[CrossRef](#)]
47. El-Dakhkhni, W.W.; Banting, B.R.; Miller, S.C. Seismic performance parameter quantification of shear-critical reinforced concrete masonry squat walls. *J. Struct. Eng.* **2013**, *139*, 957–973. [[CrossRef](#)]

Disclaimer/Publisher’s Note: The statements, opinions and data contained in all publications are solely those of the individual author(s) and contributor(s) and not of MDPI and/or the editor(s). MDPI and/or the editor(s) disclaim responsibility for any injury to people or property resulting from any ideas, methods, instructions or products referred to in the content.